Sensors and Materials, Vol. 36, No. 11 (2024) 4757–4774
MYU Tokyo

S & M 3829

Contactless Heart Rate and Heart Rate Variability Estimation Using Palm Images with Particle Swarm Optimization and Independent Component Analysis Algorithms

Te-Jen Su,[1] Wei-Hong Lin,[1] Wen-Rong Yang,[1] Ya-Chung Hung,[1]
Qian-Yi Zhuang,[1] Shih-Ming Wang,[2*] and Li-chin Tseng[1]

[1]Department of Electronic Engineering, National Kaohsiung University of Science and Technology, Kaohsiung 80782, Taiwan (R.O.C)
[2]Department of Computer Science and Information Engineering, Cheng Shiu University, Kaohsiung 833301, Taiwan (R.O.C)

(Received June 10, 2024; accepted October 11, 2024)

Keywords: particle swarm optimization algorithm, heart rate, heart rate variability, independent component analysis, contactless measurement

Since the coronavirus disease 2019 (COVID-19) pandemic, some patients with COVID-19 have experienced abnormal heart rates, posing potential health risks. In this study, we develop a noncontact method for measuring heart rate (HR) and heart rate variability (HRV) to effectively reduce the risk of infection and assist healthcare professionals in achieving accurate diagnosis and treatment. In this research, we collected data from 20 experimental testers based on palm images captured from photoplethysmography signals and measuring HR and HRV data by combining intelligent algorithms, namely, separation methods by particle swarm optimization and independent component analysis signal. The proposed method's new contactless measurement performance can effectively eliminate infection concerns and obtain HR and HRV rapidly and handily. Moreover we provide higher accuracies for physiological parameters, namely, root mean square error (2.00 bpm), mean absolute percentage error (1.5%), and measurement time (8 s), than those in recently published literature.

1. Introduction

Stress perception and cardiovascular health assessment rely on the analysis of heart rate (HR) and heart rate variability (HRV), which are crucial indicators particularly valuable for monitoring the autonomic nervous system (ANS) in surgical, critically ill, and coronavirus disease 2019 patients.[1–3] Photoplethysmography (PPG) is a noninvasive detection method, capturing changes in blood volume in living tissues through video recordings from a network camera and utilizing an active appearance model for facial landmarks and head detection.[4,5] A mathematical model for remote PPG (rPPG) measurement has been proposed on the basis of optical and physiological considerations, assuming a single light source with a constant

*Corresponding author: e-mail: k1115@gcloud.csu.edu.tw
https://doi.org/10.18494/SAM5181

ISSN 0914-4935

spectrum.[6] The analysis described in Ref. 6 reveals that combining models such as plane-orthogonal-to-skin (POS) and chrominance-bass (CHROM) rPPG, each based on different assumptions, allows the development of diverse algorithms for extracting pulse signals from video data. Extracting biometric information from facial videos involves preprocessing images through low-pass filtering and detrending. Subsequently, independent components are generated and compared, with the fast Fourier transform (FFT) employed to calculate and select the component exhibiting a significant maximum within the expected frequency range.[7] Zhang *et al.*[8] proposed using standard RGB cameras to record facial videos, extracting facial and background regions of interest (ROI) signals from each video. Joint blind source separation is then applied to eliminate standard illumination components from facial and background ROI signals, resulting in a new facial ROI signal. Independent component analysis (ICA)[9] is utilized to extract pulse signals from this new facial ROI signal, and HR is calculated using FFT.

Burton *et al.* conducted a study[10] utilizing smartphones and rPPG technology to compare signals from hairless and non-hairless skin areas. Their results revealed that rPPG measurements obtained from hairless skin areas exhibited a notable average time advantage in milliseconds as compared with those obtained from non-hairless skin areas. Moreover, pulse signal amplitudes in hairless skin areas were approximately 31% higher. The comparison of rPPG signals between these distinct regions suggested that hairless skin areas might provide more robust pulse signals, leading to more accurate measurements of HR and HRV. In a different approach, Unursaikhan *et al.*[11] proposed a methodology using a network camera to monitor RGB hue variations in the facial ROI caused by arterial pulsation for measuring interbeat intervals (IBIs). They applied wavelet transformation to extract pulse waves and calculated HRV parameters. Logistic regression analysis, incorporating these parameters during prerest, mental task, and postrest periods, was conducted to distinguish patients with major depressive disorder (MDD) from healthy volunteers. The noncontact MDD screening system demonstrated a sensitivity of 73% and a specificity of 85%, offering mental health professionals a valuable tool for preliminary assessments before taking detailed patient histories, thereby reducing the misdiagnosis rate. In a separate approach, Al Fahoum *et al.*[12] employed data mining techniques to integrate critical features of PPG signals with demographic information, allowing differentiation between healthy individuals and individuals with cardiovascular disease. This innovative method enhances diagnostic capabilities by combining physiological signals with additional patient information.

The rPPG and ICA-based BSS methods mentioned earlier exhibit prolonged convergence times, while POS and CHROM entail intricate model operations. Moreover, they primarily analyze the signal-to-noise ratio, neglecting a comprehensive discussion on the response time and accuracy of HR and HRV measurements. To circumvent these drawbacks, a method using a regular webcam to obtain continuous images, track facial landmarks, and extract regional images was developed by Su *et al.*[13] They analyzed HRV parameters in the green wavelength of the RGB color.

Space is utilized in ICA combined with particle swarm optimization (PSO) for signal elimination and obtaining physiological information through bandpass filtering, FFT, detrended fluctuation analysis (DFA), and power spectral density (*PSD*). This research is based on capturing the PPG signals of palm images and measuring HR and HRV data by combining

intelligent algorithms, namely, PSO and ICA signal separation methods. The palm image measurement method was used to replace the forehead image measurement method, and the PSO algorithm can accelerate the convergence of signal processing. In addition to preventing hair from interfering with the measurement, it can also lead to less measurement time and more accurate research results to enhance the accuracy and convenience of medical diagnosis.

The remainder of this paper is as follows. In Sect. 2, we comprehensively describe the proposed approach, elucidating its methodology and system architectural design. The experimental results obtained from applying this approach are presented and discussed in Sect. 3. Subsequently, in Sect. 4, we discuss the study's findings. Finally, our conclusions are presented in the last section, summarizing the key insights and implications drawn from the research.

2. Methodologies

In this paper, the methodologies are described as follows: to enhance computational speed and accuracy in this study, palm tracking and ROI were utilized to obtain palm images. These images were then transformed into time-domain waveforms using an average pixel approach, followed by waveform normalization. This method is preferable as it eliminates the need for complex mathematical equations.

2.1 System architecture

Figure 1 depicts the system architecture for this research. The primary objective of this study is to develop a diagnostic tool that can support healthcare professionals in diagnosing medical conditions. The system architecture is outlined as follows. Initially, an image sensor equipped with a CCD on the webcam captures images. When light is directed onto the sensor's surface, it generates electrical charges converted into voltage signals. These voltage signals are used to create and output images in real time. Subsequently, an analog-to-digital converter is employed to transform the analog voltage signals into digital ones, which are transmitted to a PC via USB serial communication. The system leverages techniques in image recognition and digital signal processing to manage and analyze significant volumes of data, ultimately extracting the user's physiological signals. The system then computes various physiological parameters, including HR and HRV, to assist healthcare providers in diagnosing medical conditions. This approach aims to enhance diagnostic efficiency and mitigate the risk of misdiagnosis.

Fig. 1. (Color online) HR and HRV measurement system.

2.2 ICA

The ICA algorithm was presented by Herault and Jutten[14] to describe the problem of blind separation systems. As specified in Eqs. (1) and (2), the observations are modeled as follows:

$$x = As\,, \tag{1}$$

where x, s, and A are the input vector, the vector of independent sources, and the merging matrix, respectively. The main target is to obtain the separating matrix W from the input vector x to form the vector of prediction sources:

$$\hat{s} = Wx\,, \tag{2}$$

where W is derived using the PSO algorithm with speed-up convergence in this paper.

A is the unknown mixing matrix, and x and s are the n-dimensional observed mixed and unknown source signals, respectively. The ICA algorithm is a generative model that describes how observation data are generated through mixing components. Independent signals cannot directly observe potential variables if the mixing matrix A is unknown. Therefore, the primary purpose of the mixing matrix A being known in Eq. (1) is to recover the unobserved independent signal source Y from the observation x.

2.3 PSO

PSO[15] is an evolutionary computation technique. Similarly to genetic algorithms, PSO is a population-based optimization tool inspired by social behavior among individuals. Each particle records the position of its previous best performance in a vector as another "best" value that is tracked by the particle swarm optimizer. Each particle calculates its velocity and updates its position in each iteration. Let x_{id} denote the best previous position encountered by the ith particle, x_{gd} denotes the global best position thus far, and t denotes the iteration counter. The current velocity of the depth dimension of the ith particle at time t is

$$v_{id}(t) = w \times v_{id}^{(t-1)} + rand_1 \times c_1 \times \left(Pbest - x_{id}^{(t-1)}\right) + rand_2 \times c_2 \times \left(Gbest - x_{id}^{(t-1)}\right). \tag{3}$$

In the above equation, *rand*() is a random function in the range [0, 1], positive constants c_1 and c_2 are personal and social learning factors, respectively, and w is the inertia weight. The new position of a particle is calculated using the following equation:

$$x_{id}^{(t+1)} = x_{id}^{t} + v_{id}^{(t+1)}. \tag{4}$$

2.4 ROI and palm images

ROI selection represents the first step in obtaining rPPG signals. It excludes nonskin regions, and most methods for measuring HR using rPPG signals require ROI selection. Choosing the palm region as the model's input for predicting rPPG signals can help eliminate interference from nonskin areas, as depicted in Fig. 2.

In this study, we employed the Palm Images functionality of MediaPipe and focused on applications in visual and audio processing.[16,17] After detecting the palm using the hand landmark model bundle, the critical point localization of 21 hand-knuckle coordinates within the detected hand regions was detected. The model was trained on approximately 30K real-world images and several rendered synthetic hand models imposed over various backgrounds, as shown in Fig. 3.[18]

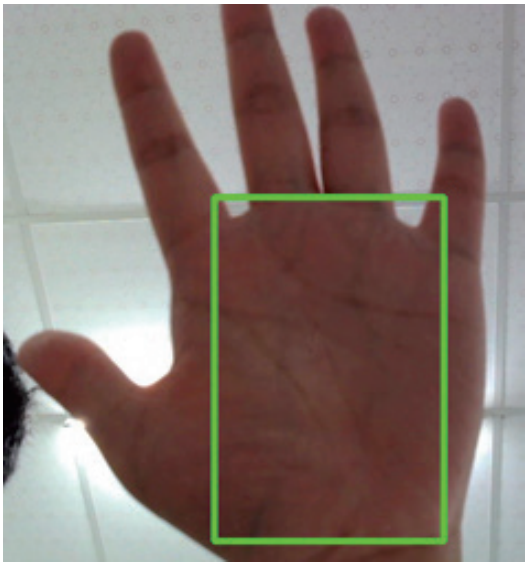

Fig. 2. (Color online) Schematic diagram of the ROI in the palm.

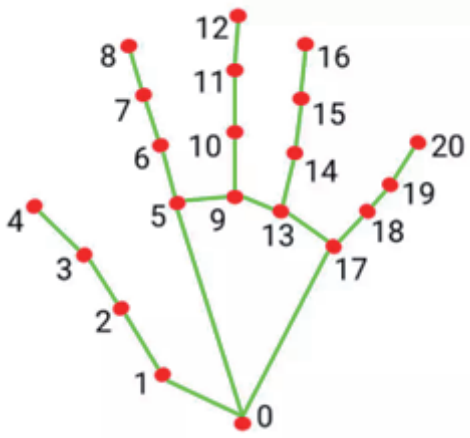

Fig. 3. (Color online) Schematic diagram of MediaPipe Palm 21 feature point mode.

2.5 HR and HRV

HR is quantified as the number of heartbeats occurring within a minute. It does not require precise timing but signifies the average beat count within a specified interval. For example, an HR of 60 beats per minute can indicate one beat per second or an average of one beat every 0.5, 1.5, 0.5, 1.5 s, and so forth.

BPM stands for beats per minute and is the unit of measurement for HR. It represents the number of heartbeats occurring in one minute. HR refers to the number of times the heart contracts and relaxes within a minute, typically expressed in BPM. For example, an HR of 60 BPM means that the heart beats 60 times per minute. HR is one of the essential indicators for assessing the overall health and cardiovascular system function and is widely used in the medical and healthcare fields.

Measuring HR typically involves analyzing the QRS complex wave in an electrocardiogram (ECG) signal, where the QRS complex represents the major visible peaks in the ECG signal. An algorithm that Pan and Tompkins proposed in 1985 is used to measure this wave.[19] This algorithm employs a 0.4–10 Hz bandpass filter to highlight the frequency content of this rapid heart depolarization and remove background noise. Subsequently, the signal is squared to enhance the QRS complex, making QRS complex identification more straightforward.

HRV measurement involves specific variations in time (or variability) between consecutive heartbeats, known as 'IBI'. Following the automatic detection of R-wave peaks in the QRS complex, ectopic heartbeats are scanned and removed to eliminate artifacts from all datasets. After this process, *RR* intervals are calculated in milliseconds. Kaufmann *et al.*[20] and Tarvainen *et al.*[21] used to obtain HRV parameters from the generated graphs. Both applications are utilized to double-check the accuracy and consistency of the results.

- **Calculation of HR and HRV parameters**

The acquired measurements necessitate conversion into interpretable values utilizing designated equations and algorithms. The ensuing time-domain parameters are specified: standard deviation of normal-to-normal intervals (*SDNN*) and root mean square of successive differences (*RMSSD*).

$$SDNN = \sqrt{\frac{\sum_{i=1}^{N}\left(RR_i - \overline{RR}\right)}{N}} \tag{5}$$

Here, RR is the period between two follow-up R-peaks of heartbeats, N is the number of RR intervals, RR_i is the period of an RR interval, and $\overline{RR}$ is the mean period of all RR intervals.

$$RMSSD = \sqrt{\frac{1}{N-1}\sum_{i=1}^{N}\left(RR_{i+1} - RR_i\right)^2} \tag{6}$$

- **HRV time domain analysis**

HRV indicates the cardiac function resulting from the intricate interaction between the cardiac system and the nonlinear processes of ANS. It is an emerging characteristic of interconnected regulatory systems that function across various time scales, aiding our adaptation to environmental and psychological challenges. It provides insights into regulating ANS balance, blood pressure, gas exchange, gastrointestinal function, heart activity, vascular tone, and more. To describe HRV, various measures are employed, including time-domain, frequency-domain, and nonlinear assessments, covering periods of 24 h, short-term intervals (5 min), or ultrashort-term durations (<5 min).

- **HRV frequency domain analysis**

The Working Group of the European Society of Cardiology and the North American Pacing and Electrophysiology Society (1996)[22] classified HRV into four frequency bands, namely, ultralow frequency (*ULF*), very low frequency (*VLF*), low frequency (*LF*), and high frequency (*HF*), with respective spectral ranges of ≤0.003, 0.0033–0.04, 0.04–0.15, and 0.15–0.40 Hz. These units serve as a quantification measure for HRV. 'Nun' denotes normalized units, which are standardization units applied to HRV.

- **Waveform processing**

rPPG measurement is often sensitive to interference from ambient light. To tackle this issue, PSO-ICA is utilized, as shown in Fig. 4, to alleviate the effect of light. Then, noise is filtered, and the signal undergoes amplification through a bandpass filter ranging from 0.4 to 10 Hz, as illustrated in Fig. 5. Subsequently, peak-to-peak detection is carried out, and the time difference between peaks is calculated using the frame rate to determine the data processing time.

- **Frequency domain transformation**

As shown in Fig. 6, after being subjected to bandpass filtering, the waveform is transformed into the frequency domain using FFT, and HR is calculated using a specified formula. The *HF* and *LF* bands are separated through the bandpass filter and then transformed into the frequency domain using *PSD*, as illustrated in Fig. 7. HRV parameters are subsequently computed using a dedicated equation.

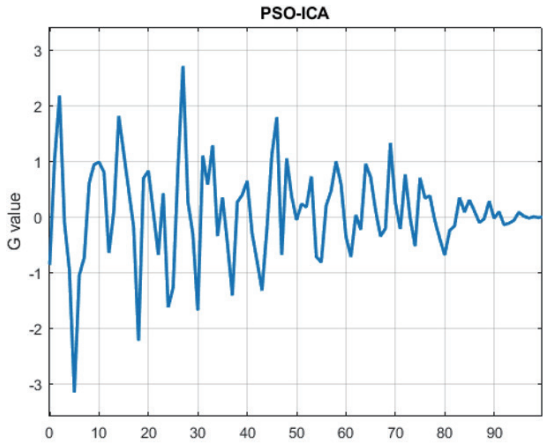

Fig. 4. (Color online) PSO-ICA waveform plot.

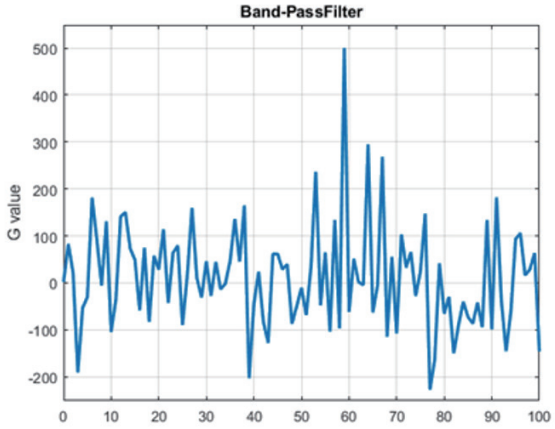

Fig. 5. (Color online) Bandpass filter waveform plot.

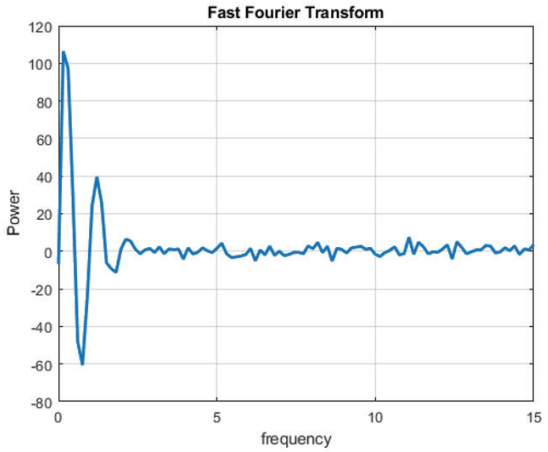

Fig. 6. (Color online) Fourier transform waveform diagram *t*.

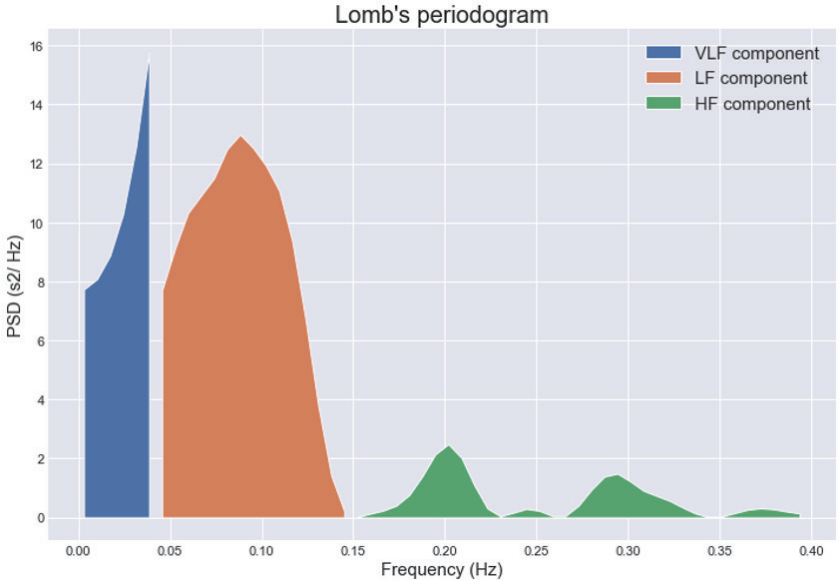

Fig. 7. (Color online) *PSD* plot.

- **Bandpass filter**

The main target of the bandpass filter is to eliminate waveform noise and narrow the feature space. Since the heart undergoes frequency variations with each heartbeat, resulting in changes in carrier frequency, in this study, we utilized the bandpass filter to isolate the carrier frequency of the heartbeat. Kohler *et al.*[23] suggested a typical frequency component range for the QRS complex of approximately 0.4 to 10 Hz. Therefore, in this study, the filter is configured within the range of 0.4–10 Hz, defining the following two frequency bands for HRV: (1) the *LF* band ranging from 0.045 to 0.15 Hz and (2) the *HF* band spanning from 0.15 to 0.4 Hz.

FFT is an expedited technique for computing the discrete Fourier transform (DFT) and is widely employed in frequency analysis. FFT analysis enables the conversion of the signal from the time domain to the frequency domain. As explained in Ref. 24, the critical difference between FFT and DFT lies in their time complexity, with FFT exhibiting a time complexity of $N\log_2(N)$ iterations, as illustrated in Eq. (7), where N represents the number of samples in the sequence.

$$x_n = \frac{1}{N}\sum_{k=0}^{N-1} X_k e^{12\pi k\frac{n}{N}}\ ,\ n = 0,\ldots,N-1 \tag{7}$$

In this research, the sequence undergoes Fourier transformation at a frequency of 10 Hz with a uniformly distributed rate. *PSD* is divided into the *VLF* (0 to 0.2 Hz), *LF* (0.20 to 0.75 Hz), and *HF* (0.75 to 3.0 Hz) bands. The spectrum for each band is estimated using the Hanning window. Subsequently, the area is computed using the trapezoidal equation, and the low-to-high-frequency power (*LF*/*HF*) ratio is determined to assess the balance between the sympathetic and parasympathetic nervous systems. The calculation of frequency domain parameters involves the trapezoidal equation $f(x)$ [Eq. (8)], which calculates the area under the *PSD* spectrum within the specified frequency domain range. The abbreviations for the frequency domain parameters are defined as follows: For HR [Eq. (9)], *VLF* represents the power within the extremely low-frequency range [Eq. (10)], *LF* represents power within the low-frequency range [Eq. (11)], and *HF* represents power within the high-frequency range [Eq. (12)].

$$\int_a^b f(x)\,dx = (b-a)\frac{f(a)+f(b)}{2} \tag{8}$$

$$HR = 60^{*}frequency \tag{9}$$

$$VLF = \int_{0.003\,\mathrm{Hz}}^{0.04\,\mathrm{Hz}} f(x)\,dx \tag{10}$$

$$LF = \int_{0.04\,Hz}^{0.15\,Hz} f(x)\,dx \tag{11}$$

$$HF = \int_{0.15\text{Hz}}^{0.4\text{Hz}} f(x)\,dx \tag{12}$$

In this investigation, normalized parameters, namely, normalized low-frequency power (*nLFP*) [Eq. (13)], normalized high-frequency power (*nHFP*) [Eq. (14)], and *LF*/*HF* ratio [Eq. (15)], are employed for validation purposes.

$$nLFP = \frac{LF}{LF + HF} \times 100\% \tag{13}$$

$$nHFP = \frac{HF}{LF + HF} \times 100\% \tag{14}$$

$$\frac{LF}{HF} = \frac{nLFP}{nHFP} \tag{15}$$

- ***PSD***

In this study, we used FFT with the Hanning window method for visualization, as demonstrated in Fig. 8.[25] The Hanning window function, represented as W(t) [Eq. (16)], was applied to enhance the mitigation of spectral energy leakage. The signal was transformed with a sampling rate of 10 Hz, and *PSD* integration was employed to categorize the signal into the following three distinct frequency bands: *VLF*: 0–0.2 Hz, *LF*: 0.20–0.75 Hz, and *HF*: 0.75–3.0 Hz. Each band featured a spectrum estimated by the Hanning window method, and the area was computed using the trapezoidal rule. Ultimately, the *LF*/*HF* ratio was determined to assess the balance between the sympathetic and parasympathetic nervous systems.

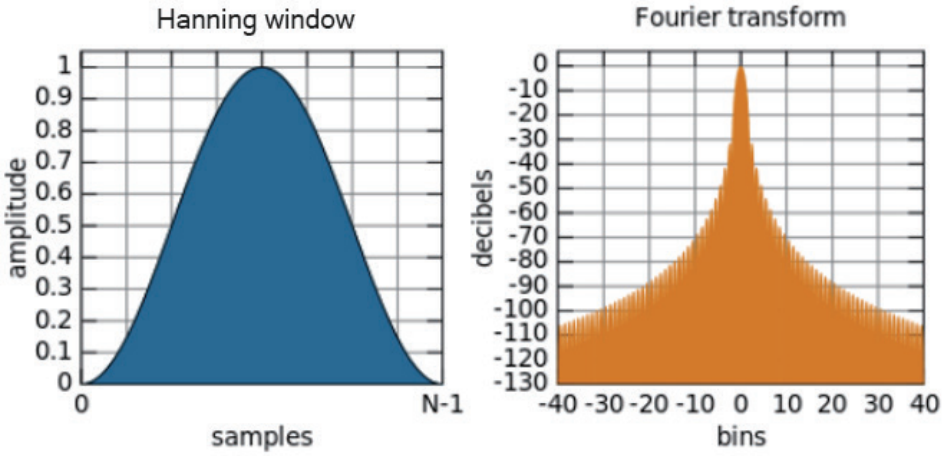

Fig. 8. (Color online) Schematic diagram of Hanning window and Fourier transform.[25]

$$W(t) = 0.5\left(1 - \cos\frac{2\pi t}{N-1}\right),\ t = 1,\ldots,N \tag{16}$$

2.6 DFA

In this study, DFA was utilized to analyze the similarity of waveforms and integrate the trends of nonstationary signals. The DFA algorithm is explained as follows: Given a time series, it can be mapped to a self-similar process through integration or summation [Eq. (17)]. First, the time length 'k' is defined, where '$\Delta t(i)$' represents the ith time interval and 'Δt' is the mean time interval. '$y(k)$' denotes the local trend. The detrending of the time series is performed using root mean square (RMS) analysis [Eq. (18)] with a length of 'n', resulting in a sequence of local linear trends. This process is repeated iteratively for DFA.

$$y(k) = \sum_{i=1}^{k}\left(x_i - x_{ave}\right) \tag{17}$$

$$F(n) = \sqrt{\frac{1}{n}\sum_{k=1}^{n}\left[y(k) - y_n(k)\right]^2} \tag{18}$$

2.7 Normalization

Normalization is the process of organizing data within a database. It has the following three main goals: unifying data scales, avoiding numerical overflow, and enhancing algorithm stability. All of these goals are valuable as they reduce the amount of space consumed by the database and ensure logical data storage. In this study, the average RGB values for each color channel within the ROI frame are calculated, and this process is repeated for each video frame. Once the video processing is complete, each color channel is saved as a signal and normalized for subsequent algorithm calculations.

2.8 Experimental environment and procedure

Figure 9 illustrates the workflow of the noncontact physiological signal measurement system developed in this study. The system has the following four main components: signal preprocessing, waveform processing, frequency domain transformation, and physiological parameter calculation. Tables 1 and 2 are the experimental environment setup and PSO parameter configuration, respectively.

(1) By utilizing the 21-point hand recognition algorithm of MediaPipe to identify hand features, the system confirms the presence of the participant's hand within the captured webcam frame. When confirmed, the system displays the image captured by the webcam, with the XY axis delineated by feature points in the ROI. The system then segments the detected area to

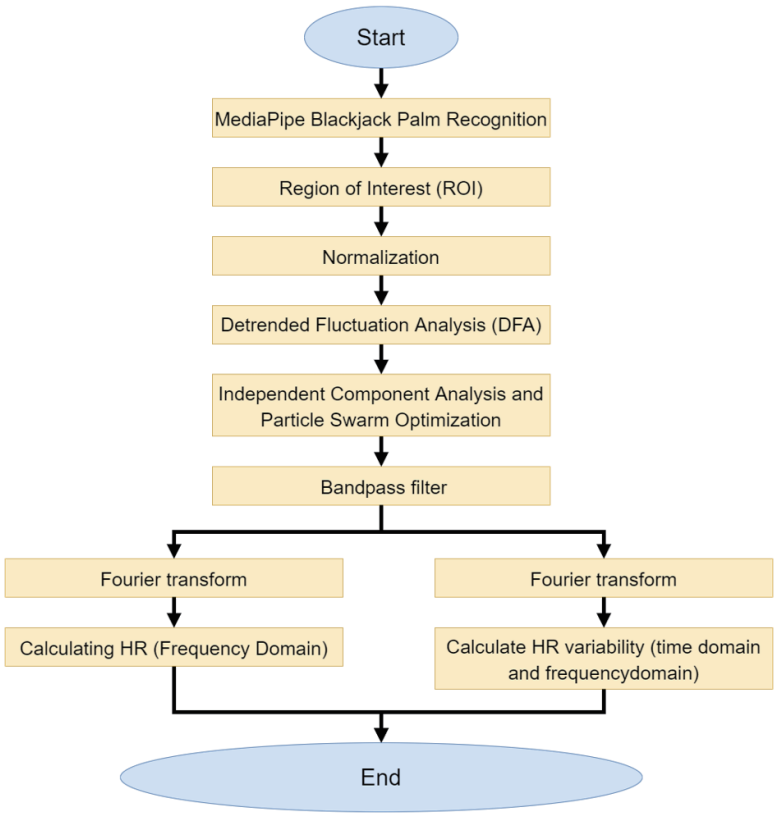

Fig. 9. (Color online) Flow chart of noncontact physiological signal measurement system.

Table 1
Experimental environment setup.

Parameters	Values
Operating system	Windows 10 (x64)
CPU	Intel(R) Core(TM) i7-9700 CPU @ 3.00 GHz
Memory	16 GB
Development environment	TensorfloW-Keras (Spyder4.2.0)
Programming language	Python3.6
Webcam	AVerMedia PW313
Dynamic resolution	1920 × 1080

Table 2
PSO parameter configuration.

Parameters	Values
Acceleration factors (c_1, c_2)	2
Inertia weight (W)	0.9
Number of iterations	20
Maximum velocity	15
Minimum velocity	8
Search maximum boundaries	−8
Search minimum boundaries	50
Random numbers (*rand*1, *rand*2)	(0, 1)
Fitness function	$Max[E\{G(w^Tz)\} - E\{G'(W^Tz)\}w]$

reduce noise interference in the analyzed images. After capturing ROI, the system separates the signals into the RGB color channels, specifically extracting the green signal. The system calculates the average of the captured green signal images, accumulating a signal sequence for each measurement, where the vertical axis represents the green signal and the horizontal axis represents the data sequence.

(2) The signals were detrended and normalized to adjust signal levels. ICA combined with PSO was employed to eliminate waveform artifacts. Subsequently, bandpass filtering was applied to extract the HR and HRV bandwidths.

(3) The waveform filtered by the bandpass filter was subjected to FFT to convert the heartbeat signal time series into the frequency domain. The peak value of the waveform was identified as the output, and *PSD* was used to represent HRV in *VLF*, *LF*, and *HF* bands.

(4) Finally, various equations and algorithms must transform the measured physiological signals into comprehensible values.

3. Results

In this study, we enlisted a cohort comprising twenty male participants aged between 20 and 30 years. The dataset was stratified on the basis of several conditions, including distances of 15 and 50 cm, ROI located on the palm, and different illuminance levels (below 200 lux, between 350 and 550 lux, and above 600 lux at a distance of 15 cm). In the subsequent sections, we will systematically present accuracy evaluation metrics, research outcomes, and data analysis specific to these experimental conditions. Finally, we will comprehensively discuss and comparatively analyze the experimental results.

- **Metrics**

The purpose of this study is to develop an auxiliary diagnostic tool, and the ultimate determination relies on pathological reports and professional medical expertise. Therefore, we employed RMS error (*RMSE*), mean absolute percentage error (*MAPE*), and the coefficient of determination (*R*-squared, R^2) as accuracy assessment metrics calculated using Eqs. (19)–(21), respectively. By observing these metrics, the system's accuracy can be assessed.

$$RMSE = \sqrt{\frac{1}{N}\sum_{i=1}^{N}\left(y_i - \widehat{y_i}\right)^2} \tag{19}$$

$$RMSE = \sqrt{\frac{1}{N}\sum_{i=1}^{N}\left(y_i - \widehat{y_i}\right)^2} \tag{20}$$

$$R^2 - 1 - \frac{\sum_{i=1}^{n}\left(y_i - \widehat{y_i}\right)^2}{\sum_{i=1}^{n}\left(y_i - \overline{y}\right)^2} \tag{21}$$

Here, y_i is the actual value of the i sample, $\widehat{y_i}$ is the measured value of the i sample, n is the total number of test samples, and $\overline{y}$ is the mean of n test samples.

- **Distance**

To analyze the accuracy of the system and the impact of ambient light on the system, we conducted actual tests on five people and compared the calculation errors of HR and HRV measured using the system and the instrument. Owing to the limited number of measurements in this study, the HR performance characteristics of two measurement distances are compared in Table 3. The higher experimental value is obtained at 15 cm.

- **Illumination**

The experimental method in this study relies on the principle of light reflection. Therefore, light intensity indirectly affects the numerical values obtained in the experiments. The following analysis is primarily intended to test the system's performance under various lighting conditions, with illuminance levels categorized below 200 lux, between 350 and 550 lux, and above 600 lux. The palm region was used for measurements at a distance of 15 cm. The measured HR represents the system's performance under various lighting conditions, and the associated errors are summarized in Table 4. As shown in Table 2, it is evident that measurements performed under an illuminance level of 350–550 lux yield superior results. In contrast, measurements conducted under extreme lighting conditions, such as complete darkness or with desk lamp supplementation, exhibited higher errors, likely due to artificially induced environmental factors. Consequently, the optimal conditions for this study involve an illuminance level between 350 and 550 lux, a measurement distance of 15 cm, and the palm as ROI for HR.

- **Measurement time**

This work uses the palm as the ROI, resulting in shorter computation times than when using the forehead. This is attributed to the reduced interference caused by hair, making images of hairless skin more advantageous in acquiring rPPG signals. The total times required for measuring physiological parameters on the palm and forehead are 8 and 10 s, respectively, resulting in a time saving of approximately 2 s.

Table 3
Comparison of HR performance characteristics of measurement at 15 and 50 cm distances.

Distance (cm)	15				50			
Metrics	Items							
	HR	*SDNN*	*LF*	*HF*	HR	*SDNN*	*LF*	*HF*
RMSE	1.10 bpm	1.85 ms	1.77%	1.77%	2.97 bpm	2.8 ms	4%	4%
MAPE (%)	1.5	4.87	2.425	3.95	3.07	8.9	6.37	8.9
R^2	0.95	0.87	0.92	0.92	0.78	0.78	0.68	0.73

Table 4
Comparison of HR performance characteristics under different lighting conditions.

Metrics	Items		
	Below 200 lumens	350–550 lumens	600 lumens or more
RMSE (bpm)	6.04	1.10	5.55
MAPE (%)	7	1.5	6
R^2	0.2843	0.9562	0.561

- **Comparisons of forehead and palm images**

The HR, *SDNN*, *LF*, and *HF* for forehead and palm images at a distance of 15 cm and an illuminance level of 350–550 lumens are compared in Table 5.

4. Discussion

We improved the algorithm method in several aspects, as demonstrated in Table 4. Table 6 shows a comparison between the algorithm method for physiological signal extraction in this study and the approaches presented in previous works by Su *et al.*,[13] Qi *et al.*,[9] and Zhang *et al.*[8] In this research, we optimized four key components, as follows:

(1) By employing DFA to adjust the waveform baseline, this algorithm enhancement can improve the accuracy of HR and HRV measurements.
(2) We introduced PSO-ICA to significantly reduce system computation time and address the issue of ICA iteratively converging to local optima under poor initial conditions.
(3) Testing the palm as an ROI confirmed that the palm image captures improved measurement accuracy and reduced the HR error to 1.5%, smaller than HR error in the measurements performed at other body parts in previous studies.
(4) The optimal measurement distance in this study is 15 cm, and the preferred illuminance falls within the range of 350–550 lumens.
(5) While most physiological parameter measurements using devices available in the market are currently performed using contact-based methods with optical volume signal description, often coupled with electrocardiography, ultrasound sensors, or piezoelectric sensors, the recent research literature has explored noncontact measurements in terms of performance and accuracy, as shown in Table 7. In this work, we used the palm as the ROI, which yielded

Table 5
Comparison of metrics for forehead and palm images.

Method	Palm images (this work)				Forehead images[13]			
Metrics	Items							
	HR	*SDNN*	*LF*	*HF*	HR	*SDNN*	*LF*	*HF*
RMSE	2.00 bpm	1.85 ms	1.77%	1.77%	2.09 bpm	2.80 ms	2.11%	2.11%
MAPE (%)	1.5	4.87	2.425	3.95	2.20	9.40	2.86	4.13
R^2	0.86	0.87	0.92	0.92	0.82	0.76	0.90	0.90

Table 6
Algorithm flow comparison table.

Function	Proposed method	Su *et al.*[13]	Qi *et al.*[9]	Zhang *et al.*[8]
ROI	Palm images	Face (partial)	Full face (with facial features)	Full face (without facial features)
Signal adjustment level	YES	YES	YES	NO
ICA	PSO-ICA	PSO-ICA	Project-ICA	JADE-ICA
Bandpass filter (Hz)	0.4–10	0.4–10	0.7–4	0.7–4
HRV equation	YES	YES	NO	NO
Continuous measurement of physiological parameter	YES	YES	YES	NO

Table 7
HR error comparison table.

	Proposed method	Su *et al.*[13]	Qi *et al.*[9]	Zhang *et al.*[8]
Measurement time (s)	8	10	30	60
HR *MAPE* (%)	1.5	2.2	5	2.5
HR *RMSE* (bpm)	1.10	1.73	6.28	2.67

higher accuracies than measurements using the forehead as the measurement area. The HR measurements proposed in this study were validated using a device approved by the Taiwan Department of Health, with an *MAPE* of 2%.

5. Conclusions

In this study, we implemented a low-cost system combining ICA with PSO for instantaneous HR and HRV estimation based on palm imaging. The palm image measurement method replaces the forehead image measurement method. In addition to eliminating hair interference on measurements, shorter measurement time and more accurate physiological parameters, namely, *RMSE* and *MAPE*, can also be obtained. In this research, we aimed to help medical professionals rapidly make appropriate diagnoses on the basis of current patient data. The new method can mitigate infection concerns and HRV rapidly and conveniently. At the same time, the method shows high accuracies for physiological parameters, namely, *RMSE* (2.00 bpm), *MAPE* (1.5%), and measurement time (8 s), compared with those in recently published papers. Future research will integrate computer vision and deep learning to investigate the measurement of relevant physiological signals.

Acknowledgments

This research is supported financially in part by the National Science and Technology Council, ROC (No. 113-2221-E-230 -004 -).

References

1 M. Trimmel: The Ergonomics Open J. **8** (2015) 32. https://doi.org/10.2174/1875934301508010032
2 D. Liao, J. Cai, F. L. Brancati, A. Folsom, R. W. Barnes, H. A. Tyroler, and G. Heiss: Diabetes Res. Clin. Pract. **30** (1995) 211. https://doi.org/10.1016/0168-8227(95)01190-0
3 D. Liao, M. Carnethon, G. W. Evans, W. E. Cascio, and G. Heiss: Diabetes **51** (2002) 3524. https://doi.org/10.2337/diabetes.51.12.3524
4 J. Allen, K. Overbeck, G. Stansby, and A. Murray: Meas. Control **39** (2006) 80. https://doi.org/10.1177/002029400603900303
5 K. Mannapperuma, B. D. Holton, P. J. Lesniewski, and J. C. Thomas: Physiol. Meas. **36** (2015) 67. https://doi.org/10.1088/0967-3334/36/1/67
6 W. Wang, A. C. den Brinker, S. Stuijk, and G. de Haan: IEEE Trans. Biomed. Eng. **64** (2017) 1479. https://doi.org/10.1109/TBME.2016.2609282
7 C. Wang, T. Pun, and G. Chanel: Front. Bioeng. Biotechnol. **6** (2018) 33. https://doi.org/10.3389/fbioe.2018.00033
8 B. Zhang, H. Li, L. Xu, L. Qi. Lin, Y. Yao, and S. E. Greenwald: J. Sens. **2021** (2021) 18. https://doi.org/10.1155/2021/9995871

9 L. Qi, H. Yu, L. Xu, R. Mpanda, and S. E. Greenwald: Physiol Meas. **40** (2019) 085007. https://doi.org/10.1088/1361-6579/ab2c9f
10 T. Burton, G. Saiko, M. Cao, and A. Douplik: Proc. 2022 IEEE Photonics Conf. (IPC, 2022) 1–2. https://doi.org/10.1109/IPC53466.2022.9975569
11 B. Unursaikhan, N. Tanaka, G. Sun, S. Watanabe, M. Yoshii, K. Funahashi, F. Sekimoto, F. Hayashibara, Y. Yoshizawa, L. Choimaa, and T. Matsui: Front. Physiol. **12** (2021) 1. https://doi.org/10.3389/fphys.2021.642986
12 A. S. Al Fahoum, A. O. Abu Al Haija, and H. A. Alshraideh: Bioengineering **10** (2023) 249. https://doi.org/10.3390/bioengineering10020249
13 T.-J. Su, Y.-C. Hung, T.-S. Pan, W.-H. Lin, S.-M. Wang, and Y.-C. Lee: Appl. Sci. **13** (2023) 7605. https://doi.org/10.3390/app13137605
14 J. Herault and C. Jutten: AIP Conf. Proc. **151** (1986) 206. https://doi.org/10.1063/1.36258
15 R. Poli, J. Kennedy, and T. Blackwell: Swarm Intell. **1** (2007) 33. https://doi.org/10.1007/s11721-007-0002-0
16 C. Lugaresi, J. Tang, H. Nash, C. McClanahan, E. Uboweja, M. Hays, F. Zhang, C.-L. Chang, M. G. Yong, J. Lee, W.-T. Chang, W. Hua, M. Georg, and M. Grundmann: arXiv preprint (2019) 1. https://doi.org/10.48550/arXiv.1906.08172
17 Google AI Blog: https://research.google/blog/mediapipe-holistic-simultaneous-face-hand-and-pose-prediction-on-device/ (accessed January 2023).
18 F. Zhang, V. Bazarevsky, A. Vakunov, A. Tkachenka, G. Sung, C.-L. Chang, and M. Grundmann: arXiv preprint (2020) 1. https://doi.org/10.48550/arXiv.2006.10214
19 J. Pan and W. J. Tompkins, IEEE Trans. Biomed. Eng. **BME-32** (1985) 230. https://doi.org/10.1109/TBME.1985.325532
20 T. Kaufmann, S. Sütterlin, S. M. Schulz, and C. Vögele: Behav. Res. Methods **43** (2011) 1161. https://doi.org/10.3758/s13428-011-0107-7
21 M. P. Tarvainen, J.-P. Niskanen, J. A. Lipponen, P. O. Ranta-ahoa, and P. A. Karjalainen: Comput. Methods Programs Biomed. **113** (2014) 210. https://doi.org/10.1016/j.cmpb.2013.07.024
22 A. H. Kemp, D. S. Quintana, M. A. Gray, K. L. Felmingham, K. Brown, and J. M. Gatt: Biol. Psychiatry **67** (2010) 1067. https://doi.org/10.1016/j.biopsych.2009.12.012
23 B.-U. Kohler, C. Hennig, and R. Orglmeister: IEEE Eng. Med. Biol. **21** (2022) 42. https://doi.org/10.1109/51.993193
24 O. M. Essenwanger: Elements of Statistical Analysis (Elsevier, Amsterdam, 1986).

About the Authors

Te-Jen Su received his Ph.D. degree in electrical engineering from National Cheng-Kung University Tainan, Taiwan, in 1989. He is currently a professor at the Department of Electronic Engineering, National Kaohsiung University of Applied Sciences, Kaohsiung, Taiwan. His research interests include intelligent control systems, AI algorithm applications, and satellite communication systems. (sutj@nkust.edu.tw)

Wei-Hong Lin received his Master of Science in Optoelectronics, degree, from National Sun Yat-sen University in 1998. He is a Ph.D. student at the National Kaohsiung University of Science and Technology, Department of Electronic Engineering. He has worked in the R&D department of the Lite-On Technology Corporation, TOPSOC Semiconductor Company, and Microchip Technology Inc., and has more than 20 years of experience in product development. (i110152102@nkust.edu.tw)

Wen-Rong Yang is a Ph.D. student at the National Kaohsiung University of Science and Technology, Department of Electronic Engineering, and an assistant research fellow, the Marine Industry and Engineering Research Center. (i110152105@nkust.edu.tw)

Ya-Chung Hung received his master's degree in electronic engineering from the National Kaohsiung University of Science and Technology in 2016. He is a Ph.D. student at the National Kaohsiung University of Science and Technology, Department of Electronic Engineering. He works at the Air Force Institute of Technology as a teacher, at Air Force General Headquarters as a major, and at the First Logistics Command of the Air Force as a radio repair officer. (aaa13y@gmail.com)

Qian-Yi Zhuang received his master's degree in electronic engineering from the National Kaohsiung University of Science and Technology in 2024. He is a Ph.D. student at the National Kaohsiung University of Science and Technology, Department of Electronic Engineering. He specialized in signal processing, industrial communications, artificial intelligence, biological signal processing, and firmware research and development. (j111252102@nkust.edu.tw)

Shih-Ming Wang received his Master's and Ph.D. degrees from the Department of Electronic Engineering, National Kaohsiung University of Science and Technology, Taiwan, in 2015 and 2020, respectively. He crosses several professional fields including biological and medical engineering, electrical and electronic engineering, and information engineering. He is currently with the Department of Computer Science and Information Engineering, Cheng Shiu University, Kaohsiung, Taiwan. His research interests include artificial intelligence, automatic control, bioinformatics, biomedical engineering, computational intelligence, embedded systems, electric and hybrid vehicles, Internet of Things, machine learning, mobile medical, power electronics, renewable energy, robotics, and smart healthcare. (k1115@gcloud.csu.edu.tw)

Li-chin Tseng received his master's degree in electronic engineering from the National Kaohsiung University of Science and Technology in 2023. (f110152183@nkust.edu.tw)